## Title

Assessment of Reynolds stress components and turbulent pressure loss using 4D flow MRI with extended motion encoding



## Journal

Magnetic Resonance in Medicine, 79(4)

## ISSN

0740-3194

## Authors

Haraldsson, Henrik
Kefayati, Sarah
Ahn, Sinyeob
et al.

## Publication Date

2018-04-01

## DOI

10.1002/mrm.26853

Peer reviewed

HHS Public Access

Author manuscript

*Magn Reson Med*. Author manuscript; available in PMC 2019 April 01.

Published in final edited form as:

*Magn Reson Med*. 2018 April ; 79(4): 1962–1971. doi:10.1002/mrm.26853.

# Assessment of Reynolds Stress Components and Turbulent Pressure Loss using 4D flow MRI with Extended Motion Encoding

**Henrik Haraldsson**[1,†], **Sarah Kefayati**[1,†], **Sinyeob Ahn**[2], **Petter Dyverfeldt**[3], **Jonas Lantz**[3], **Matts Karlsson**[3], **Gerhard Laub**[2], **Tino Ebbers**[3], and **David Saloner**[1,4]

[1]University of California, San Francisco, United States

[2]Siemens Healthcare

[3]Linköping University, Linköping, Sweden

[4]Veterans Affairs Medical Center, San Francisco, CA, USA

## Abstract

**Purpose—**To measure the Reynolds stress tensor using 4D flow MRI, and to evaluate its contribution to computed pressure maps.

**Methods—**A method to assess both velocity and Reynolds stress using 4D flow MRI is presented and evaluated. The Reynolds stress is compared by cross-sectional integrals of the Reynolds stress invariants. Pressure maps are computed using the Pressure Poisson Equation - both including and neglecting the Reynolds stress.

**Result—**Good agreement is seen for Reynolds stress between computational CFD, simulated MRI, and MRI experiment. The Reynolds stress can significantly influence the computed pressure loss for simulated (e.g. −0.52% vs −15.34% error, $p<0.001$) and experimental (e.g. 306±11 vs 203±6 Pa, $p<0.001$) data. A 54% greater pressure loss is seen at the highest experimental flow rate when accounting for Reynolds stress ($p<0.001$).

**Conclusion—**4D flow MRI with extended motion-encoding enables quantification of both the velocity and the Reynolds stress tensor. The additional information provided by this method improves the assessment of pressure gradients across a stenosis in the presence of turbulence. Unlike conventional methods which are only valid if the flow is laminar, the proposed method is valid for both laminar and disturbed flow, a common presentation in diseased vessels.

### Keywords

Turbulence; Phase contrast MRI; Hemodynamics; pressure loss; MR flow Imaging; arterial stenosis

Corresponding Author. Henrik Haraldsson. VAMC/UCSF, Radiology 114-D, Bldg 203, Rm BA-51, 4150 Clement Street, San Francisco, CA 94530. Phone: +1(415)-2214810 ext 3815. Henrik.Haraldsson@ucsf.edu.

†These authors contributed equally to this work.

## Introduction

Irreversible pressure loss is a major determinant for evaluating the hemodynamic impact of valvular and vascular stenosis. Currently, invasive catheterization is used to measure pressure loss, but this method is not frequently used as catheterization is invasive with an associated risk for bleeding [1], clotting, and infections [2]. There are also inaccuracies in pressure measurements due to variability in the precise positioning of the catheter [3] and the influence of the catheter on the blood flow [4]. A non-invasive method to accurately measure irreversible pressure loss would potentially improve the assessment of the hemodynamic significance in valvular and vascular stenosis and reduce patient discomfort.

Irreversible pressure loss across significant stenoses is primarily caused by turbulence dissipation. Clinically, non-invasive assessment of the pressure loss is most often performed by Doppler ultrasound combined with the simplified Bernoulli equation [5]. This approach provides an estimate of the maximum pressure gradient [6], effectively assuming that the pressure loss is irreversible. However, the pressure commonly recovers after the stenosis, especially if the stenosis is mild to moderate. Another promising approach is velocity measurements using 3D cine phase-contrast magnetic resonance imaging (4D flow MRI) in combination with the pressure-Poisson equation. It provides a relative pressure field that takes only the laminar part of the flow into account [7–9]. However, all these approaches neglect turbulent flow effects.

Recent developments in 4D flow MRI permit estimation of not only the laminar, mean component of the velocity field but also the turbulent, fluctuating component [10–12]. This approach permits estimation of the variance of velocity within a voxel and the turbulent kinetic energy (TKE). TKE estimation has been explored for the estimation of irreversible pressure loss across a stenosis [13]. However, full characterization of turbulence and the associated pressure loss requires estimation of the complete Reynolds stress tensor that includes not only variances but also covariances of the velocity within a voxel. Accurate quantification of these components is also important in the investigation of turbulent forces on blood constituents [14].

The current MR turbulence mapping method allows measurement of the velocity variance in three perpendicular directions, that correspond to the diagonal components of the Reynolds stress tensor [10]. Estimation of velocity covariance from a combination of multiple acquisitions has been attempted [15], but has so far been limited to one component and has not resulted in accurate results. In this study, we aimed to develop an MR turbulence mapping method with extended motion encoding for the estimation of the complete Reynolds stress tensor. The stress tensor was then used to estimate the irreversible pressure loss that is associated with turbulent flow.

## Methods

### ICOSA6 4D flow MRI Theory

The estimation of velocity variance in 4D flow MRI is similar to the approach used in diffusion weighted imaging (DWI) [16]. DWI has been furthered by using non-orthogonal,

multi-directional encoding schemes to obtain the full tensor, a technique referred to as diffusion tensor imaging (DTI). One encoding scheme for DWI is defined by the nodes of an Icosahedral (ICOSA) Polyhedra using 6 encoding directions (ICOSA6) [17] – an encoding scheme that will be described in more detail below. Non-orthogonal multi-directional encodings are of little value for conventional (orthogonal encoding) 4D flow MRI studies as the velocity will be overdetermined. However, a recent study suggested these non-orthogonal encoding schemes as an alternative to dual-VENC acquisitions as they provide better velocity-to-noise ratios [18].

We propose the use of the novel ICOSA6 motion encoding scheme to acquire the three-directional mean velocity and the full Reynolds stress tensor. The ICOSA6 motion-encoding scheme includes one flow compensated reference and 6 motion encodings, each directed towards different nodes of an icosahedron as described in Table 1.

The Reynolds stress tensor can be obtained from ICOSA6 motion-encoded data using the following equation:

$$k_{i,\nu}\tau_{ij}k_{j,\nu} = -2ln\left(\left|\frac{S(k_\nu)}{S(0)}\right|\right) \quad (1)$$

Here $k_v$ denotes the velocity sensitivity vector $[\gamma M_{1,x}, \gamma M_{1,y}, \gamma M_{1,z}]^{\mathrm{T}}$. For $N$ motion encodings we obtain a system of $N$ equations:

$$\begin{bmatrix} k_{x,1}^2 & k_{y,1}^2 & k_{z,1}^2 & k_{x,1}k_{y,1} & k_{x,1}k_{z,1} & k_{y,1}k_{z,1} \\ k_{x,2}^2 & k_{y,2}^2 & k_{z,2}^2 & k_{x,2}k_{y,2} & k_{x,2}k_{z,2} & k_{y,1}k_{z,2} \\ \vdots & \vdots & \vdots & \vdots & \vdots & \vdots \\ k_{x,N}^2 & k_{y,N}^2 & k_{z,N}^2 & k_{x,N}k_{y,N} & k_{x,N}k_{z,N} & k_{y,N}k_{z,N} \end{bmatrix} \begin{bmatrix} \tau_{xx} \\ \tau_{yy} \\ \tau_{zz} \\ \tau_{xy} \\ \tau_{xz} \\ \tau_{yz} \end{bmatrix} = \begin{bmatrix} -2\ln\left(\left|\frac{S(k_1)}{S(0)}\right|\right) \\ -2\ln\left(\left|\frac{S(k_2)}{S(0)}\right|\right) \\ \vdots \\ -2\ln\left(\left|\frac{S(k_N)}{S(0)}\right|\right) \end{bmatrix} \quad (2)$$

Equation 2 allows us to calculate the Reynolds stress for an arbitrary motion encoding given that, 1) it includes a flow compensated acquisition with zero first gradient moment, and 2) the column rank of the encoding matrix is at least 6. ICOSA6 encoding and the flow-compensated reference acquisition fulfils both of these requirements and allows us to solve the system of equations to obtain both the variances, $\tau_{XX}$, $\tau_{yy}$, and $\tau_{zz}$, and the covariances, $\tau_{Xy}$, $\tau_{Xz}$, and $\tau_{yz}$, of the Reynolds stress tensor.

Phase unwrapped phase-difference images and subsequent velocity images were obtained from the ICOSA6 motion-encoded data by using a slightly modified version of the approach described by Zwart et al [18]. By defining a matrix providing the directions of the motion encodings

$$P = \begin{bmatrix} -1/\sqrt{1+\psi^2} & 0 & \psi/\sqrt{1+\psi^2} \\ 1/\sqrt{1+\psi^2} & 0 & \psi/\sqrt{1+\psi^2} \\ -\psi/\sqrt{1+\psi^2} & 1/\sqrt{1+\psi^2} & 0 \\ -\psi/\sqrt{1+\psi^2} & -1/\sqrt{1+\psi^2} & 0 \\ 0 & \psi/\sqrt{1+\psi^2} & 1/\sqrt{1+\psi^2} \\ 0 & -\psi/\sqrt{1+\psi^2} & 1/\sqrt{1+\psi^2} \end{bmatrix} \quad (3)$$

an encoding matrix $E$ can then be written as

$$E = P \cdot \pi / venc \quad (4)$$

In the case of unaliased velocities $E$ relates the true velocity $V=[V_x, V_y, V_z]^T$ to the phases $\varphi=[\varphi_1, \varphi_2, \varphi_3, \varphi_4, \varphi_5, \varphi_6]^T$.

$$\varphi = EV \quad (5)$$

The Moore-Penrose pseudoinverse is used solve the overdetermined problem of computing three velocities from the six phases, and the sum of squared residuals $S$ serves as a measure of consistency of the solution:

$$S(\varphi) = \|(EE^{+} - I)\varphi\|_2 \quad (6)$$

where $^+$ denotes the Moore-Penrose pseudoinverse. Phase unwrapping can be performed by finding the most consistent unwrapped solution within $n$ phase wraps by solving

$$\min_k S(\varphi + 2\pi k) \quad (7)$$

where $k=[k_1,k_2,k_3,k_4,k_5,k_6]$ denotes the number of phase unwraps (integer) and $|2\pi k_i|<n$. The Moore-Penrose pseudoinverse is used to obtain the unwrapped velocities from the unwrapped phase.

## Flow Model

A flow model was constructed that consisted of a rigid pipe with an unconstricted diameter of 15 mm and a cosine-shaped stenosis with a maximal area reduction of 75%. The stenotic pipe was inserted in a flow loop that included a computer-controlled step motor that pumped water through the model at programmable rates. The water was doped with Gd-DTPA to shorten the longitudinal relaxation time, $T_1$. Six different step motor setting were used, and

the flow rates were determined from the 4D flow acquisitions. Flow rates and Reynolds numbers are summarized in Table 2.

## CFD Simulation

As Reynolds stress cannot be measured directly, the components of the Reynolds stress tensor and the pressure field were calculated in CFD simulation for two flow conditions to serve as a reference standard. The flow was computed numerically by solving the Navier-Stokes equations in ANSYS CFX 16.0. Inflow profiles were obtained for 45.3 ml/s and 22.0 ml/s flowrates while a constant relative static pressure was set at the outlet. The walls were considered rigid and the no-slip condition was imposed. The fluid was water with a constant density of 997 $kg/m^3$ and a dynamic viscosity of $8.899 \cdot 10^{-4}$ kg/ms. The computational meshes were created in ANSYS ICEM 16.0 and consisted of 12 million high quality anisotropic hexahedral cells. The highest mesh density was in the immediate post-stenotic region and the thickness of the mesh cells close to the wall grew exponentially by a factor of 1.05 until it matched the mesh size in the center of the stenosis. The time step was 50μs, and global imbalances of mass and momentum were always less than 0.1%, which ensured that the simulation was performed with sufficient accuracy.

Turbulent flow fluctuations were resolved using Large Eddy Simulation (LES), a technique that resolves the large energy-carrying turbulent scales and models the small isotropic scales where energy dissipation occurs. As such, the components in the Reynolds stress tensor can be computed from the flow field. Sampling of flow statistics started after initial transient startup effects had disappeared. The LES technique has previously been validated against direct numerical simulations (DNS) for this type of flow [19].

## Simulation of MR data

The CFD data for the 45.3 ml/s flow rate was further processed to simulate ICOSA6 4D flow data. This was achieved by computing velocity and Reynolds stress components along the ICOSA6 velocity encoding directions for each CFD cell. The phase and signal loss as seen by an ICOSA6 4D flow encoding were computed using the relation described in Equation 5 and 1, resulting in a complex value for each CFD cell. The complex values were interpolated using a Gaussian weighting with a standard deviation equal to the voxel resolution divided by 2.35 [20] to produce voxels for simulated MR datasets. Simulated MR data was computed for the 45.3 ml/s flow rate for a range of VENCs, ranging from 0.55m/s to 1.15m/s and spatial resolutions ranging from 0.8mm to 1.6mm. Complex noise was added to the simulated MR data to obtain SNRs ranging from 2 to 80. 100 samples were produced for each combination of VENC and resolution for each SNR, see Supporting Table S1. All datasets were processed with the post processing method described below. Background correction was omitted for the simulated MR data due to the absence of phase offsets and the lack of reference tissue.

## MRI Data Acquisition

The flow model was placed on the MRI patient table with the stenotic segment close to the center of the magnet. Saline bags doped with Gd-DTPA were placed around the model to permit background correction.

The ICOSA6 motion encoding scheme was implemented by replacing the orthogonal motion encoding scheme in a conventional 4D flow MRI sequence. The motion encoding, flow rate and Reynolds number are listed in Table 2. 4D flow MRI was performed using the following imaging parameters: a flip angle of 15°, 110×192×20 mm field of view, matrix size of 92×160×40, voxel size of 1.2×1.2×1.2 mm. The echo and repetition times ranged from 3.64–3.96ms and 5.49–5.81ms, respectively.

## Post Processing

The ICOSA6 4D flow MRI data was post-processed using an in-house script written in Python. The post-processing steps used to obtain the velocities and the Reynolds stress tensor included:

1. Subtraction of the reference phase from the motion-encoded phases to remove phase accrual by other factors than velocity encoding.
2. Background phase offset correction on the subtracted phase images using a second-order polynomial soft fitting to stationary tissue [21]. This step was omitted for the simulated datasets.
3. Automatic unwrapping of the phase using shared information between non-orthogonal velocity measurements using Equation 7. The phase was unwrapped within the region $|\varphi|<1.8\pi$ - an interval determined ad hoc.
4. Computation of the Reynolds stress using Equation 2.

## Pressure Poisson Equation

4D flow MRI velocity data has previously been used to compute relative pressure fields using the pressure Poisson equation (PPE) [7] under the assumption that the flow is 1) incompressible, 2) Newtonian, 3) steady (laminar), and 4) without external body forces. Under these assumptions, the mean relative pressure is obtained by solving the following PPE:

$$\nabla^2 p_{negl} = \nabla \cdot (-\rho \boldsymbol{V} \cdot \nabla \boldsymbol{V} + \mu \nabla^2 \boldsymbol{V}) \quad (8)$$

where $p_{negl}$ is the pressure computed by neglecting the turbulence, $\rho$ is the density, $\boldsymbol{V}$ is the velocity, and $\mu$ is the viscosity.

As ICOSA6 enables us to obtain the full Reynolds stress tensor, it is no longer necessary to assume laminar flow. The PPE can therefore be derived from the Reynolds-averaged Navier-Stokes equation (RANS), in which the velocities have been decomposed into their average and fluctuating components. Under the assumption that the flow is 1) incompressible, 2) Newtonian, and 3) without external forces, the mean relative pressure can then be obtained by solving the following PPE:

$$\nabla^2 p_{incl} = \nabla \cdot (-\rho \boldsymbol{V} \cdot \nabla \boldsymbol{V} - \rho \nabla \boldsymbol{\tau} + \mu \nabla^2 \boldsymbol{V}) \quad (9)$$

where $p$ is the pressure, and $\boldsymbol{\tau}$ is the Reynolds stress components describing the fluctuating parts of the velocity field.

The relative pressure field in the phantom was solved three times: once assuming laminar flow, $p_{negl}$ (Equation 8); once including the Reynolds stresses, $p_{incl}$ (Equation 9); once only including the contribution of the Reynolds stresses in regions where the TKE surpassed a 0.02 J/kg threshold, $p_{thresh}$. The 0.02 threshold was determined ad hoc to limit noise in the Reynolds stresses to influence the pressure estimation. The PPE was solved using radial basis function generated finite differences [22] with a stencil including the 7 closest voxels within the flow regime.

### Evaluation

**Reynolds Stress—**Three rotational invariants of the Reynolds stress tensor, IA=tr($\boldsymbol{\tau}$), IIA =(tr($\boldsymbol{\tau}$)$^2$−tr($\boldsymbol{\tau}^2$))/2, and IIIA=det($\boldsymbol{\tau}$), were computed for both MRI and CFD data, and these invariants were integrated over cross-sectional slices along the pipe. We note that the first invariant is proportional to the turbulent kinetic energy (TKE).

**Pressure Loss—**The pressure loss was extracted along the centerline of the CFD data, the simulated MRI, and for the MRI acquisitions. For the simulated MRI and the acquired MRI this produced three pressure curves, $p_{negl}$, $p_{incl}$, and $p_{thresh}$.

## Results

### MRI Simulation

The simulated data showed that the ICOSA6 velocity encoding scheme is able to assess the Reynolds stresses. Figure 1 shows the velocities, Reynolds stresses and the pressure loss from the CFD simulation as well as for a simulated MRI dataset using an isotropic resolution of 1.2mm, a VENC of 0.85m/s, and a SNR of 20. Note an overall good agreement of the CFD and the simulated MRI. The larges error in the Reynolds stress components are seen in the $\tau_{XX}$ component at the border of the jet, and the standard deviations of the Reynolds components are greatest in the turbulent region. An underestimation of the pressure loss is apparent when neglecting the Reynolds stress in the pressure computation, $p_{negl}$. Greater standard deviation in the pressure is seen in the turbulent region.

The cross-sectional integrals of the Reynolds stress invariants in the simulated MRI express the same features as the CFD, as seen in Figure 2. The invariants dependency to SNR, resolution, and VENC are illustrated in Supporting Figure S1–S3, where an overall elevation of the IA invariant can be seen as the SNR decreases and to a lesser degree as the VENC increases.

The influence of including the Reynolds stress in the pressure computations is illustrated in pressure curves extracted along the centerline of the pipe, as shown in Figure 3. Pressure curves for a range of SNRs, resolutions, and VENCs are shown in Supporting Figure S4–S6. The difference in pressure loss computed by the three methods was compared using a paired Wilcoxon rank-sum test. Significant differences of the absolute error of the three methods are seen for most resolutions, VENCs, and SNRs, as summarized in Supporting Table S1.

The influence of VENC, resolution, and SNR were compared for each of the three methods. Significant differences were seen when changing these parameters (pairwise Wilcoxon rank-sum test) – these differences were however small in certain ranges of these parameters, e.g. SNR≥10, resolution≤1.2mm, and VENC≥0.70m/s as illustrated in Figure 4, 5, and 6 respectively.

### MRI Acquisitions

An MRI acquisition performed at the same flow rate as the CFD simulation illustrates similar features as the simulated MRI data, e.g. the largest errors in the Reynolds stress components are seen in the $\tau_{XX}$ component at the border of the jet, as well as the smaller pressure loss obtained when neglecting the Reynolds stress in the pressure computation, as illustrated in Figure 7.

The MRI acquisition also shows how both the cross-sectional Reynolds components and the pressure losses increase with the flow rate, as shown in Figure 8. Significant differences in pressure loss between the three methods of computing the pressure loss were seen at the higher flow rates (presented in detail in Supporting Table S2). Note that $p_{thresh}$ presents pressure losses similar to $p_{negl}$ at the lower flow rate, whereas at higher flowrates it presents values closer to $p_{incl}$.

## Discussion

A method is presented that uses 4D flow MRI with extended motion encoding to quantify the Reynolds stress tensor. Additionally, the Reynolds stresses have been included to improve pressure assessment using 4D flow. The main findings of this study are: 1) 4D flow with extended motion encoding can be used to assess the Reynolds stress. The Reynolds stress acquired with this method agrees with CFD simulations of the flow. 2) By including the Reynolds stress in the MRI based pressure computation we are able to estimate the partial pressure recovery that occurs in the presence of turbulence. In a flow experiment with a 51ml/s flow rate, accounting for the Reynolds stress (as is proposed in this work) showed a 54% greater pressure loss than was found when the Reynolds stress was neglected (the conventional method in 4D flow.)

The proposed method may contribute to the investigation of flow-induced blood damage and to the computation of relative pressure maps. For the former, the contribution of the laminar viscous stress on constituents of blood can be calculated from the velocity alone; however, by using the method presented in this work the viscous stress resulting from turbulence can also be taken into account. For the latter, clinical non-invasive assessment of pressure loss has known limitations. The simplified Bernoulli assumes that the kinetic energy of the jet is lost in turbulence and that no pressure recovery occurs after the jet. This assumption can lead to an overestimation of the net pressure loss in mild to moderate stenosis. Computing pressure from velocity alone using the PPE, on the other hand, does account for the pressure recovery but neglects the turbulence. This leads to an overestimation of the recovery in the presence of turbulence. The method presented in this work is able to account for both the pressure recovery and the turbulence, and could therefore contribute to the investigation of

pathologies such as the clinically relevant mild to moderate stenosis by improving non-invasive measurement of pressure loss.

As expected, the pressure obtained using both simulated and acquired ICOSA6 4D flow data showed some dependence on SNR, VENC, and resolution. The major cause of this dependence is incorrectly unwrapped data which has a direct impact on the pressure computation. Unwrapping becomes more challenging as the SNR decreases and the VENC is set lower, explaining some of the large errors and standard deviation seen in Supporting Table S1 (e.g. for VENC 0.55m/s and for most cases with SNR<15). Too coarse resolution may also make it challenging to capture the spatial features of the flow, and could be responsible for the errors seen for 1.4mm and 1.6mm isotropic resolution. $p_{thresh}$ is seen to be relatively consistent for cases where SNR≥10, resolution≤1.2mm, and VENC≥0.70m/s.

The expression for computing the Reynolds stress, as derived in this work, is generic and does not rely on the ICOSA6 encoding scheme. This encoding scheme has however been proposed as suitable for diffusion tensor imaging [17], which is intrinsically similar to the method to quantify the Reynolds stress tensor presented here. In many cases, the optimal VENC for velocity and turbulence estimation differs. However, ICOSA6 has a reduced VENC-sensitivity when compared with conventional 4-point velocity encoding. This is because a non-orthogonal encoding schemes such as the ICOSA6 encoding scheme can use shared information to automatically unwrap the velocity [18], making it possible to base the selection of VENC on the turbulence rather than on the velocity.

A limitation of this study is the unavoidable differences between the experimental setup used for the 4D flow acquisition and the idealized CFD simulation, a difference that is most notably observed by differences in the length of the jet. While this difference results in an extended pressure plateau in the CFD simulation, it does not change the agreement of the net pressure loss caused by the stenosis. Another limitation is the use of stationary flow. However, the technique can readily be applied to pulsatile in vivo flow, analogously to the time-resolved acquisition of turbulence [13] and pressure computation [8]. Pulsatile flow would require including the temporal derivative of the velocity in the PPE:

$$\nabla^2 p = \nabla \cdot \left( -\rho \frac{\partial \boldsymbol{V}}{\partial t} - \rho \boldsymbol{V} \cdot \nabla \boldsymbol{V} - \rho \nabla \boldsymbol{\tau} + \mu \nabla^2 \boldsymbol{V} \right) \quad (10)$$

The temporal derivative could, as done in previous works [7,8], be computed directly from the time resolve velocity data.

## Conclusion

4D flow with extended motion encoding is able to not only quantify the normal Reynolds stress components, but the full Reynolds stress tensor as well as complete velocity data. Utilizing these measurements for pressure estimation provides greatly improved pressure loss estimates. Accurate estimation of pressure losses has the potential to impact clinical decision-making in pathologies such as aortic stenosis and coarctation.

## Supplementary Material

Refer to Web version on PubMed Central for supplementary material.

## Acknowledgments

Grant Support: Supported by the European Research Council through Heart4flow,Grant nr 310612 (TE), and by the National Institutes of Health through HL114118 (DS) and NS059944 (DS).

## References

1. Doyle BJ, Ting HH, Bell MR, Lennon RJ, Mathew V, Singh M, et al. Major Femoral Bleeding Complications After Percutaneous Coronary Intervention. JACC Cardiovasc Interv. 2008; 1:202–9. DOI: 10.1016/j.jcin.2007.12.006 [PubMed: 19463301]
2. Muñoz P, Blanco JR, Rodríguez-Creixéms M, García E, Delcan JL, Bouza E. Bloodstream Infections After Invasive Nonsurgical Cardiologic Procedures. Arch Intern Med. 2001; 161:2110.doi: 10.1001/archinte.161.17.2110 [PubMed: 11570940]
3. Nishimura RA, Carabello BA. Hemodynamics in the Cardiac Catheterization Laboratory of the 21st Century. Circulation. 2012; 125:2138–50. DOI: 10.1161/CIRCULATIONAHA.111.060319 [PubMed: 22547754]
4. Imbesi SG, Kerber CW. Pressure Measurements across Vascular Stenoses: Practice and Pitfalls. Interv Neuroradiol. 1999; 5:139–44. DOI: 10.1177/159101999900500205 [PubMed: 20670502]
5. Nishimura RA, Otto CM, Bonow RO, Carabello BA, Erwin JP, Guyton RA, et al. 2014 AHA/ACC Guideline for the Management of Patients With Valvular Heart Disease. J Am Coll Cardiol. 2014; 63:e57–185. DOI: 10.1016/j.jacc.2014.02.536 [PubMed: 24603191]
6. Hatle L, Angelsen BA, Tromsdal A. Non-invasive assessment of aortic stenosis by Doppler ultrasound. Br Heart J. 1980; 43:284–92. [PubMed: 7437175]
7. Tyszka JM, Laidlaw DH, Asa JW, Silverman JM. Three-dimensional, time-resolved (4D) relative pressure mapping using magnetic resonance imaging. J Magn Reson Imaging JMRI. 2000; 12:321–9. [PubMed: 10931596]
8. Ebbers T, Farnebäck G. Improving computation of cardiovascular relative pressure fields from velocity MRI. J Magn Reson Imaging JMRI. 2009; 30:54–61. DOI: 10.1002/jmri.21775 [PubMed: 19557846]
9. Goubergrits L, Riesenkampff E, Yevtushenko P, Schaller J, Kertzscher U, Hennemuth A, et al. MRI-based computational fluid dynamics for diagnosis and treatment prediction: Clinical validation study in patients with coarctation of aorta: MRI-Based CFD Diagnosis. J Magn Reson Imaging. 2015; 41:909–16. DOI: 10.1002/jmri.24639 [PubMed: 24723299]
10. Dyverfeldt P, Sigfridsson A, Kvitting J-PE, Ebbers T. Quantification of intravoxel velocity standard deviation and turbulence intensity by generalizing phase-contrast MRI. Magn Reson Med Off J Soc Magn Reson Med Soc Magn Reson Med. 2006; 56:850–8. DOI: 10.1002/mrm.21022
11. Dyverfeldt P, Kvitting J-PE, Sigfridsson A, Engvall J, Bolger AF, Ebbers T. Assessment of fluctuating velocities in disturbed cardiovascular blood flow: In vivo feasibility of generalized phase-contrast MRI. J Magn Reson Imaging. 2008; 28:655–63. DOI: 10.1002/jmri.21475 [PubMed: 18777557]
12. Dyverfeldt P, Gårdhagen R, Sigfridsson A, Karlsson M, Ebbers T. On MRI turbulence quantification. Magn Reson Imaging. 2009; 27:913–22. DOI: 10.1016/j.mri.2009.05.004 [PubMed: 19525079]
13. Dyverfeldt P, Hope MD, Tseng EE, Saloner D. Magnetic Resonance Measurement of Turbulent Kinetic Energy for the Estimation of Irreversible Pressure Loss in Aortic Stenosis. JACC Cardiovasc Imaging. 2013; 6:64–71. DOI: 10.1016/j.jcmg.2012.07.017 [PubMed: 23328563]
14. Grigioni M, Daniele C, D'Avenio G, Barbaro V. Evaluation of the surface-averaged load exerted on a blood element by the Reynolds shear stress field provided by artificial cardiovascular devices. J Biomech. 2002; 35:1613–22. DOI: 10.1016/S0021-9290(02)00234-8 [PubMed: 12445614]

15. Elkins CJ, Alley MT, Saetran L, Eaton JK. Three-dimensional magnetic resonance velocimetry measurements of turbulence quantities in complex flow. Exp Fluids. 2009; 46:285–96. DOI: 10.1007/s00348-008-0559-4

16. Taylor DG, Bushell MC. The spatial mapping of translational diffusion coefficients by the NMR imaging technique. Phys Med Biol. 1985; 30:345–9. [PubMed: 4001161]

17. Hasan KM, Parker DL, Alexander AL. Comparison of gradient encoding schemes for diffusion-tensor MRI. J Magn Reson Imaging. 2001; 13:769–80. DOI: 10.1002/jmri.1107 [PubMed: 11329200]

18. Zwart NR, Pipe JG. Multidirectional high-moment encoding in phase contrast MRI. Magn Reson Med. 2013; 69:1553–63. DOI: 10.1002/mrm.24390 [PubMed: 22760964]

19. Gårdhagen R, Lantz J, Carlsson F, Karlsson M. Large Eddy Simulation of Stenotic Flow for Wall Shear Stress Estimation - Validation and Application. WSEAS Trans Biol Biomed. 2011; 8:86–101.

20. Casas B, Lantz J, Dyverfeldt P, Ebbers T. 4D flow MRI-Based pressure loss estimation in stenotic flows: Evaluation using numerical simulations: Pressure Loss Estimation in Stenotic Flows Using 4D Flow MRI. Magn Reson Med. 2015; :n/a–n/a. DOI: 10.1002/mrm.25772

21. Ebbers T, Haraldsson H, Dyverfeldt P, Sigfridsson A, Warntjes MJB, Wigström L. Higher order weighted least-squares phase offset correction for improved accuracy in phase-contrast MRI. ISMRM. 2008

22. Wright GB, Fornberg B. Scattered node compact finite difference-type formulas generated from radial basis functions. J Comput Phys. 2006; 212:99–123. DOI: 10.1016/j.jcp.2005.05.030

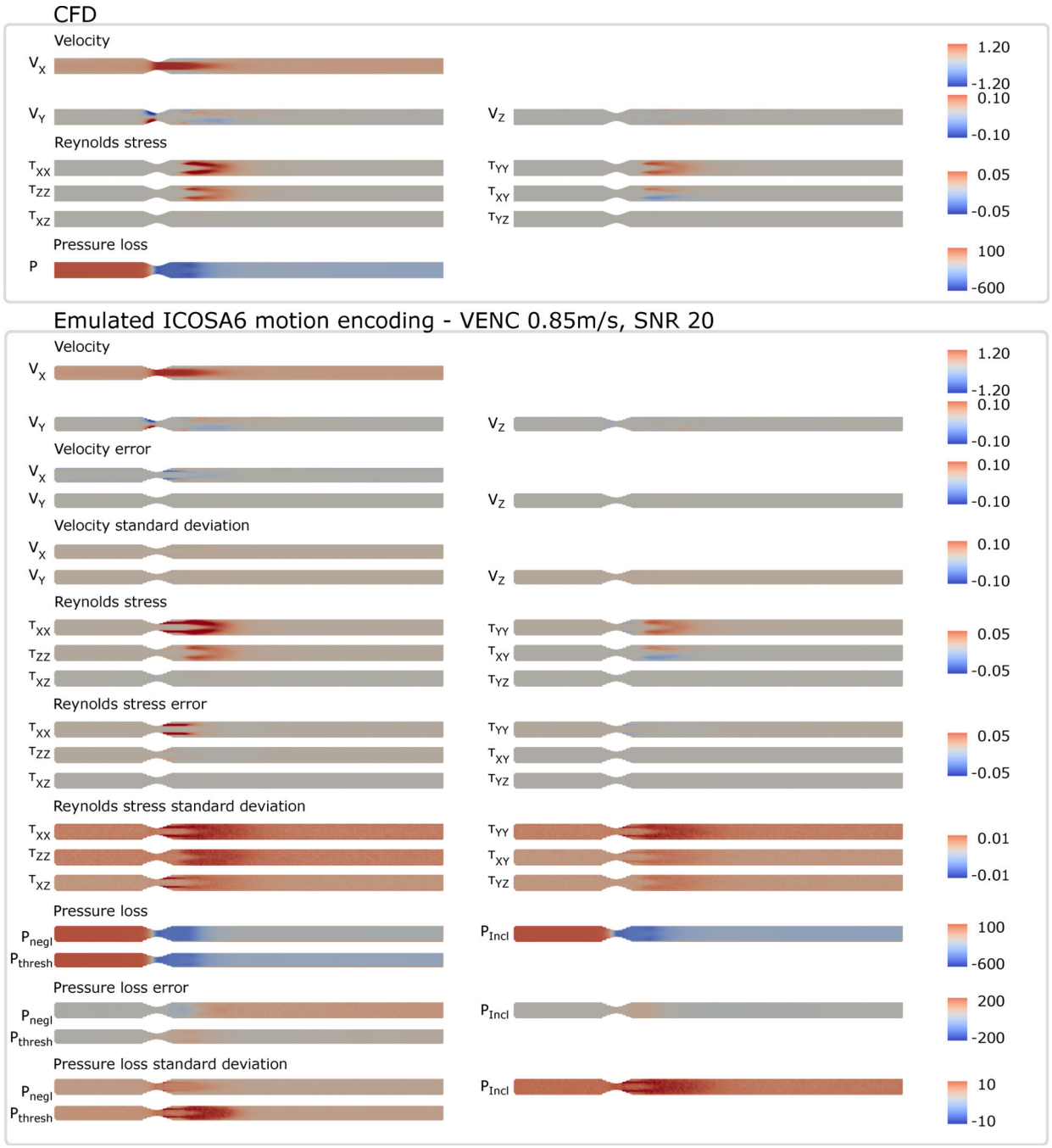


**Figure 1.**

The velocities, Reynolds stress and relative pressure map along the pipe for the 45ml/s flow rate. Upper panel shows the result from the CFD simulation. Lower panel shows the result obtain while simulating an 4D flow acquisition using ICOSA6 motion encoding with a VENC of 0.85m/s with an SNR of 20. Note the good agreement between the pressure map of the CFD simulation and the pressure map obtained from the simulated ICOSA6 4D flow data when including the Reynolds stresses.

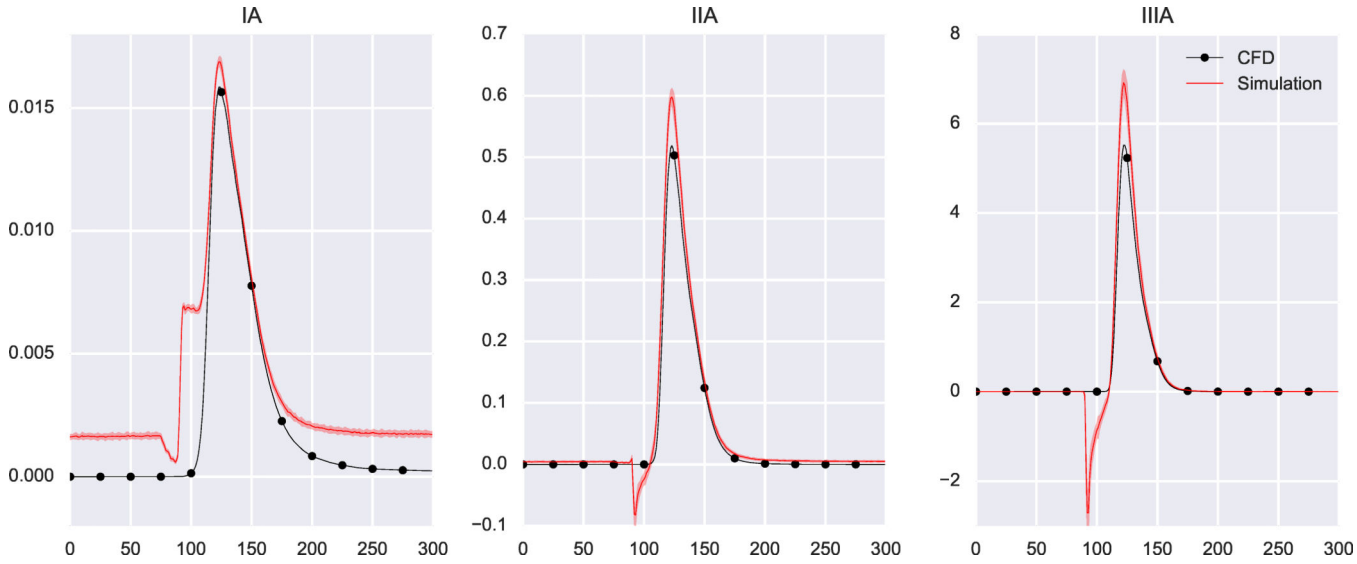


**Figure 2.**

Cross-sectional integrals of the Reynolds stress invariants along the centerline of the pipe. The black lines marked with dots show the result from the CFD simulation, whereas the red lines show results obtained from a simulated ICOSA6 4D flow acquisition with a SNR of 20, a 1.2mm isotropic resolution, and a VENC of 0.85m/s. Invariants for additional values of SNR, resolution, and VENC are found in the supplementary material.

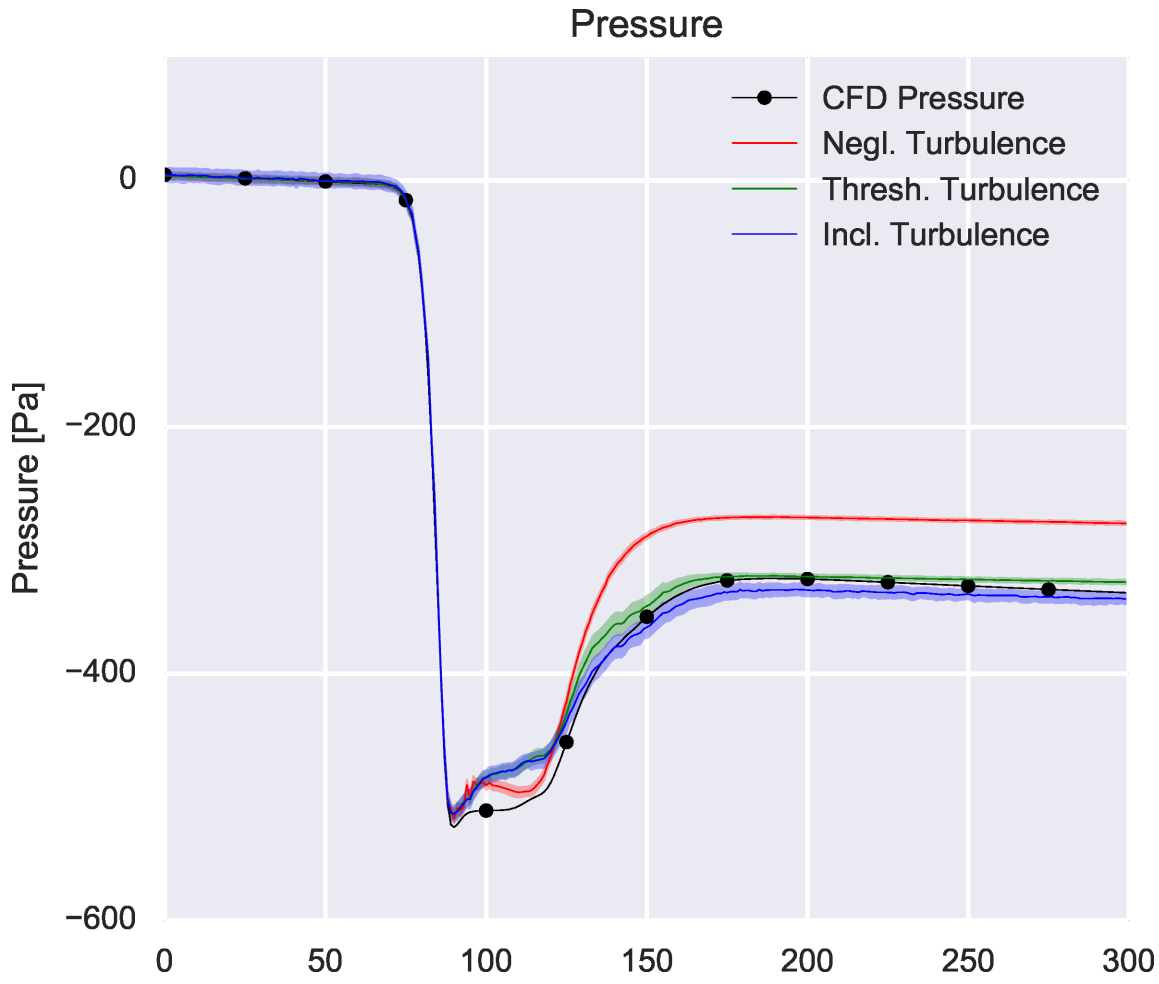


**Figure 3.**

Pressure profile along the centerline of the pipe. The black line marked with dots shows the pressure profile from the CFD simulation. The colored lines show the pressure profiles obtained from a simulated ICOSA6 4D flow acquisition with a SNR of 20, a 1.2mm isotropic resolution, and a VENC of 0.85m/s estimation - when neglecting Reynolds stress (red), when including Reynolds stress (blue), and when including Reynolds stress in regions with TKE>0.02 J/kg (green). Pressure profiles for additional values of SNR, resolution, and VENC are found in the supplementary material.

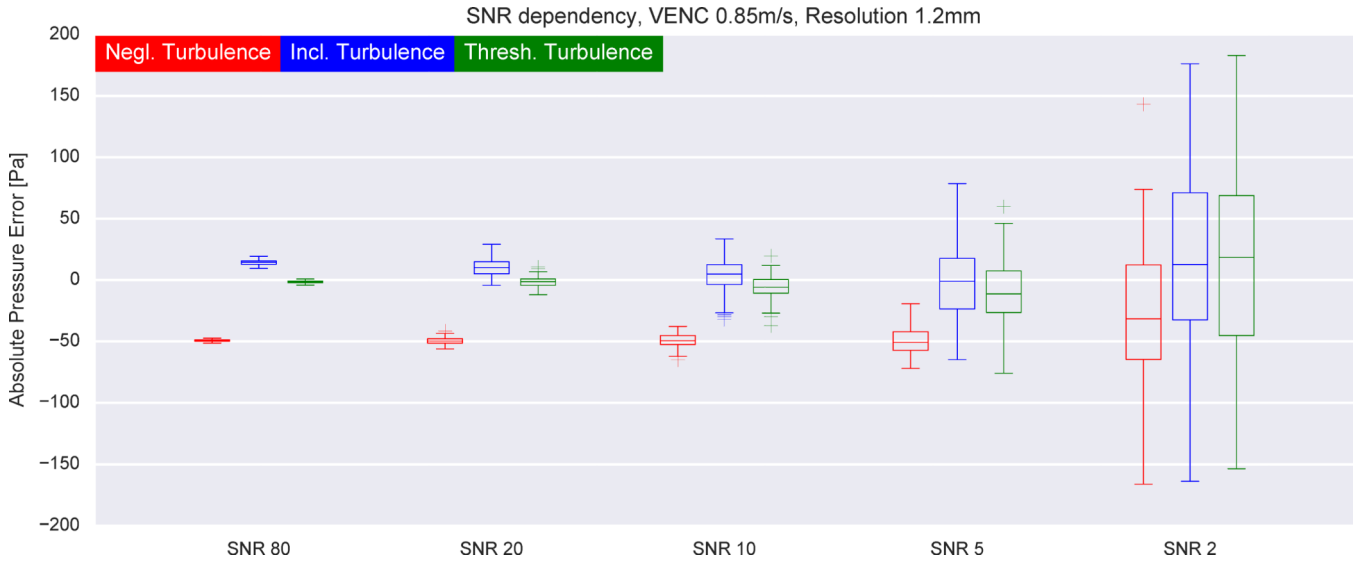


**Figure 4.**

The figure shows the SNR dependency of the pressure loss estimation - when neglecting Reynolds stress (red), when including Reynolds stress (blue), and when including Reynolds stress in regions with TKE>0.02 J/kg (green).

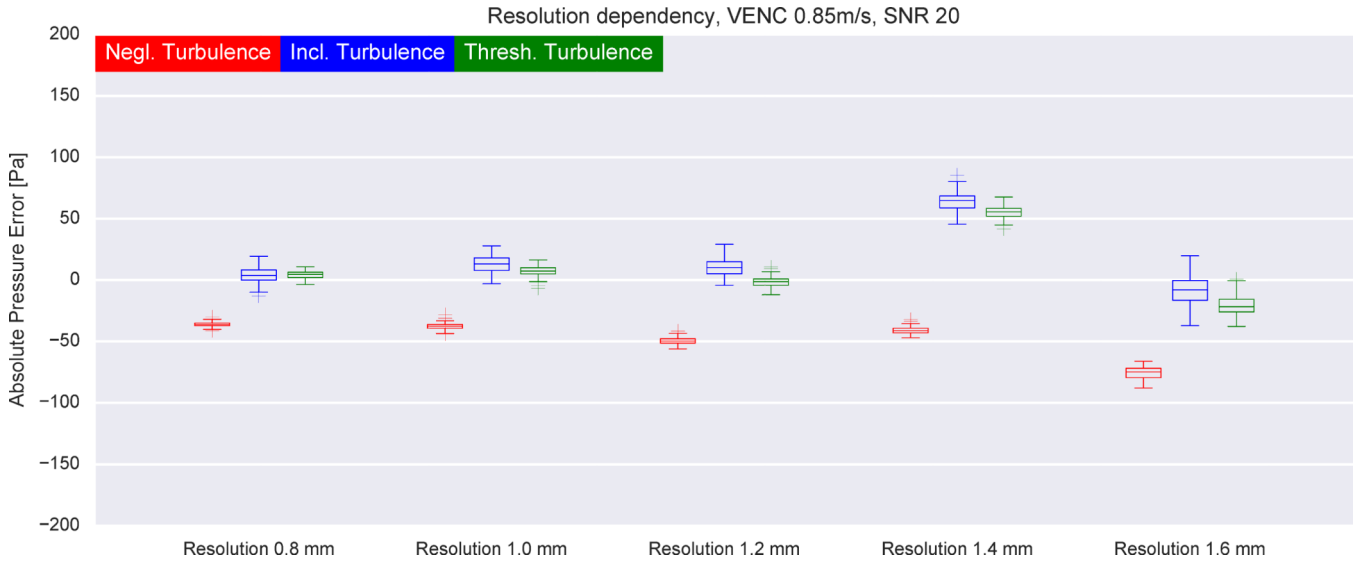


**Figure 5.**

The figure shows the resolution dependency of the pressure loss estimation - when neglecting Reynolds stress (red), when including Reynolds stress (blue), and when including Reynolds stress in regions with TKE>0.02 J/kg (green).

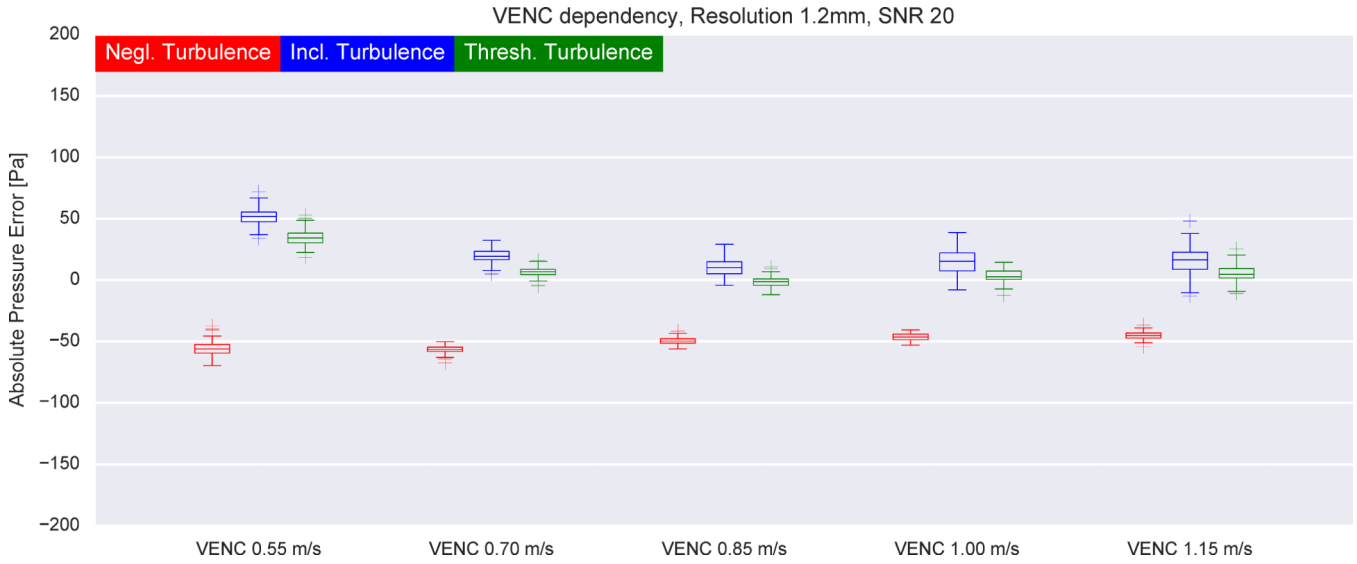


**Figure 6.**

The figure shows the VENC dependency of the pressure loss estimation - when neglecting Reynolds stress (red), when including Reynolds stress (blue), and when including Reynolds stress in regions with TKE>0.02 J/kg (green).

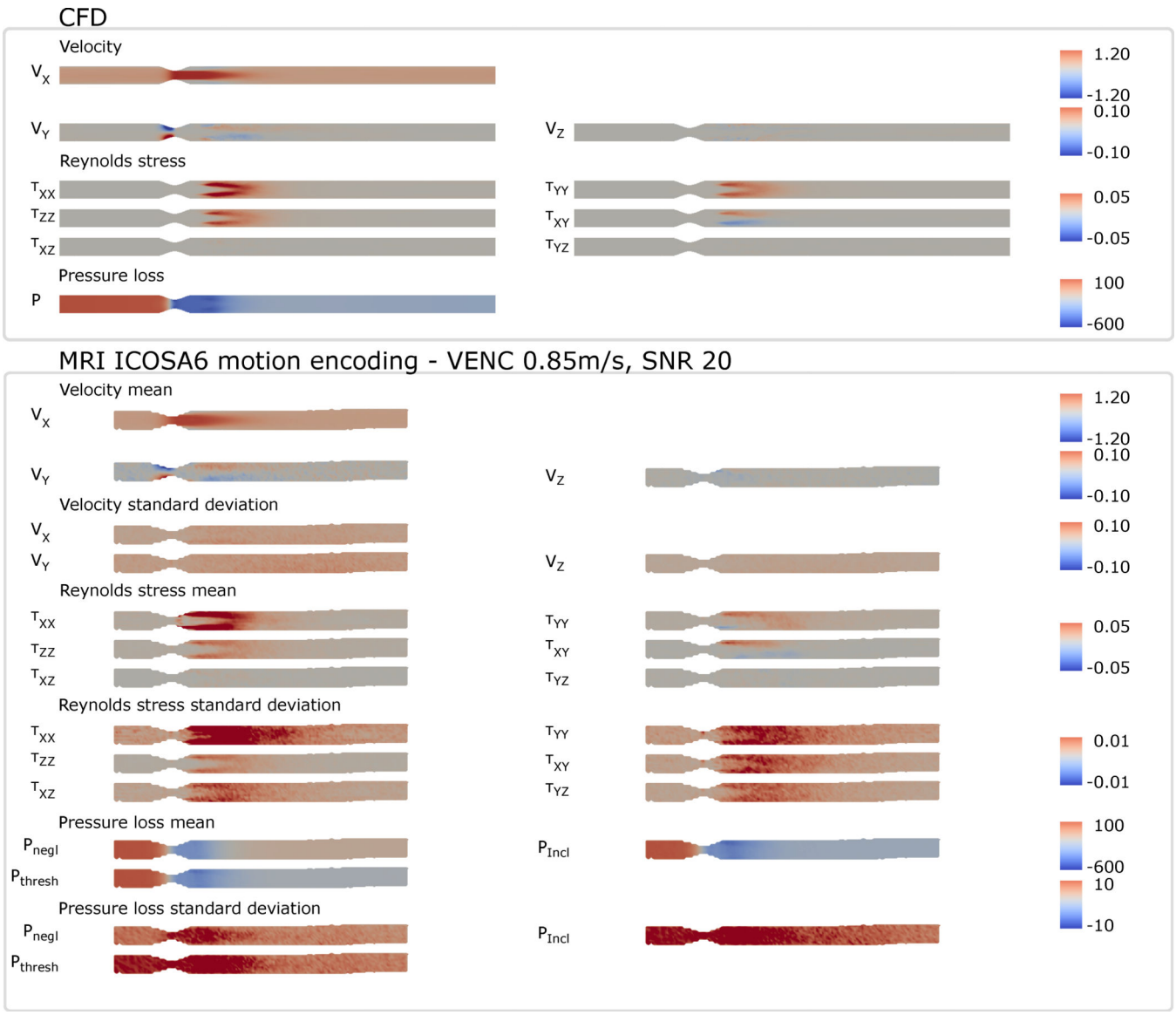


**Figure 7.**

The lower panel shows the velocity, Reynolds stress, and relative pressure map obtained using a flow phantom. Upper panel shows the CFD simulation of a matching flow rate. Note the good agreement between the relative pressure map of the CFD and those obtained from in the flow phantom when accounting for the Reynolds stress.

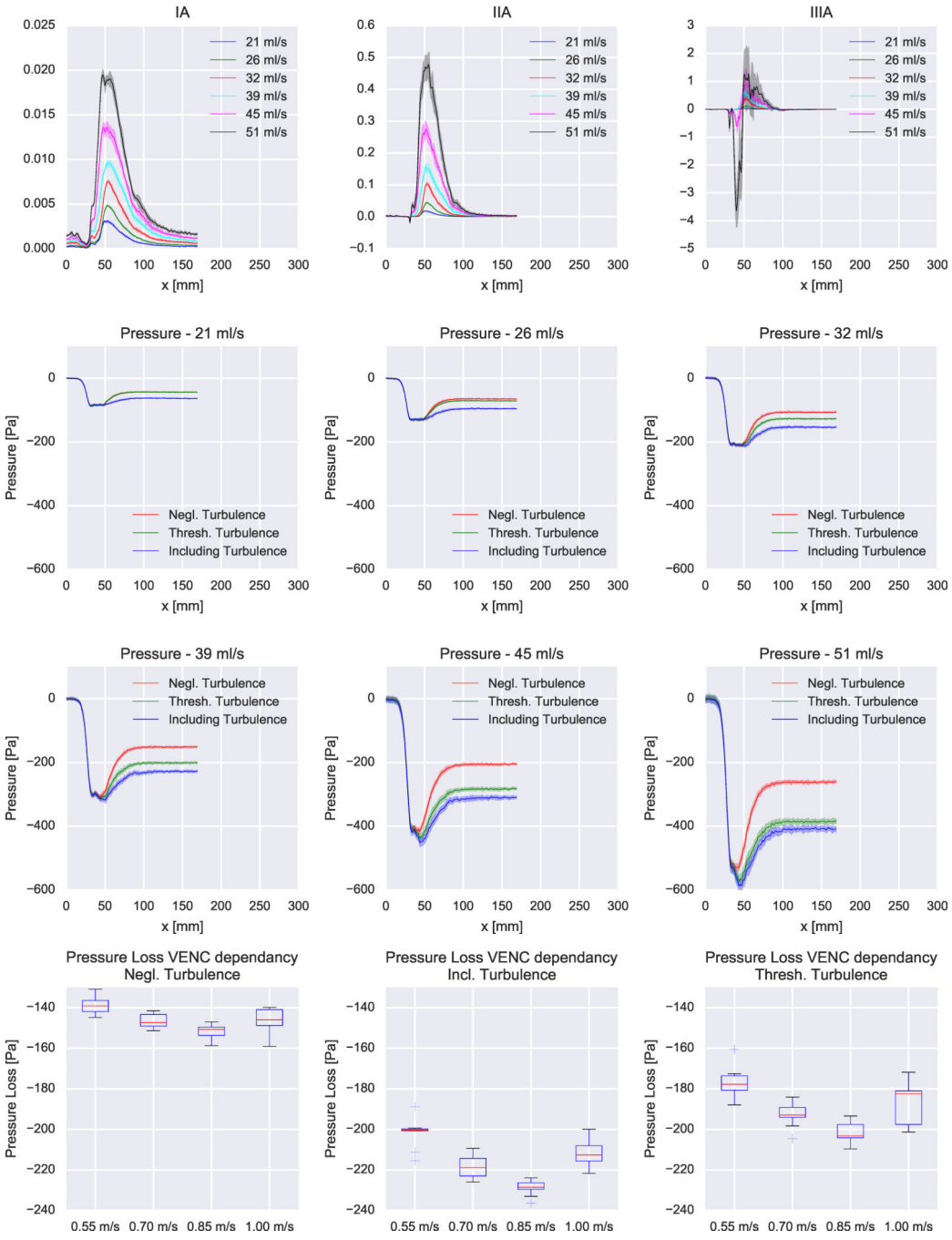


**Figure 8.**

The top panel shows how the cross-sectional integrals of the Reynolds stress invariants increase with increase flow rate in the flow phantom. Middle panel shows the pressure profile along the center line for different flow rate. The panel illustrates that increased flow rate increases the pressure loss over the stenosis. It further illustrates that the pressure recovery is greater, i.e. the net pressure loss is smaller, when turbulence is neglected. The

bottom panel shows the VENC dependency of the estimated pressure loss for the 39ml/s flow rate.

**Table 1**

ICOSA6 encoding scheme. The encoding uses the golden ratio $\Psi=(1+\mathrm{sqrt}(5))/2$ to evenly distribute the encoding directions over a hemisphere.

| Encoding | $\mathbf{M}_{1,\mathrm{readout}}$ | $\mathbf{M}_{1,\mathrm{phase}}$ | $\mathbf{M}_{1,\mathrm{slice}}$ |
|---|---|---|---|
| 0 | 0 | 0 | 0 |
| 1 | $-1/\mathrm{sqrt}(1+\psi^2)$ | 0 | $\psi/\mathrm{sqrt}(1+\psi^2)$ |
| 2 | $1/\mathrm{sqrt}(1+\psi^2)$ | 0 | $\psi/\mathrm{sqrt}(1+\psi^2)$ |
| 3 | $-\psi/\mathrm{sqrt}(1+\psi^2)$ | $1/\mathrm{sqrt}(1+\psi^2)$ | 0 |
| 4 | $-\psi/\mathrm{sqrt}(1+\psi^2)$ | $-1/\mathrm{sqrt}(1+\psi^2)$ | 0 |
| 5 | 0 | $\psi/\mathrm{sqrt}(1+\psi^2)$ | $1/\mathrm{sqrt}(1+\psi^2)$ |
| 6 | 0 | $-\psi/\mathrm{sqrt}(1+\psi^2)$ | $1/\mathrm{sqrt}(1+\psi^2)$ |

**Table 2**

Summary of flow and imaging parameters

| Flow rate [ml/s] | 21 | 26 | 32 | 39 | 45 | 51 |
|---|---|---|---|---|---|---|
| **Reynolds number** | **2000** | **2470** | **3040** | **3710** | **4280** | **4850** |
| Motion encoding [m/s] | 0.45 | 0.55 | 0.70 | 0.55<br>0.70<br>0.85<br>1.00 | 1.00 | 1.15 |